

Cationic surfactant templated synthesis of magnetic mesoporous nanocomposites for efficient removal of Light Green

Beyhan Erdem^{*,†}, Sezer Erdem^{**}, and Nalan Tekin^{***}

*Department of Chemistry, Faculty of Science and Arts, Bursa Uludag University, 16059, Bursa, Turkey

**Department of Physics, Faculty of Science and Arts, Bursa Uludag University, 16059, Bursa, Turkey

***Department of Chemistry, Faculty of Science and Arts, Kocaeli University, 41380, Kocaeli, Turkey

(Received 25 December 2020 • Revised 26 April 2021 • Accepted 29 April 2021)

Abstract— $\text{Fe}_3\text{O}_4\text{-SiO}_2\text{-NH}_2$, $\text{Fe}_3\text{O}_4\text{-CTABSiO}_2\text{-NH}_2$ and $\text{Fe}_3\text{O}_4\text{-SiO}_2\text{-CTABSiO}_2\text{-NH}_2$ magnetic adsorbents were successfully prepared and could be used effectively for the adsorption of Light Green from aqueous solutions. Unlike the first sample, mesoporous silica coatings were created using cetyltrimethylammoniumbromide micelles as molecular templates on superparamagnetic iron oxide in one sample, and on silica-coated iron oxide in the other sample to improve the adsorptive properties of the nanocomposites. The characterization by FT-IR, SEM/EDX, Zeta-potential, XRD, VSM, and N_2 -adsorption/desorption confirmed the production of mesoporous silica layer. Although coating processes with both silica and mesoporous silica layers led to a vaguely decrease in saturation magnetization of the $\text{Fe}_3\text{O}_4\text{-SiO}_2\text{-CTABSiO}_2\text{-NH}_2$, the nanoparticles were protected with silica coatings for environment conditions and made more suitable for subsequent amino functionalization. The results determined from Batch adsorption experiments fitted to Langmuir isotherm model with maximum adsorption capacity (q_{max}) equal to 56.18, 196.08 and 227.27 mg g^{-1} , for $\text{Fe}_3\text{O}_4\text{-SiO}_2\text{-NH}_2$, $\text{Fe}_3\text{O}_4\text{-CTABSiO}_2\text{-NH}_2$ and $\text{Fe}_3\text{O}_4\text{-SiO}_2\text{-CTABSiO}_2\text{-NH}_2$, respectively, and it was seen from the kinetic results, the LG adsorption was identified by pseudo-second-order kinetics, revealing that LG adsorption process is homogeneous, monolayer and based on chemical interactions. According to the results, both silica and mesoporous silica coating strategy can play crucial role in improving the adsorptive properties of nanocomposites.

Keywords: Light Green, Nanocomposite, Magnetite, Mesoporous Silica, CTAB

INTRODUCTION

Synthetic organic dyes are released from varied chemical industries such as cosmetics, paper, textile, food, leather, printing, pharmaceuticals, plastics, and paint [1,2]. It is estimated that approximately 10-15% of dye used are loss during different processes as well as in the dyeing [3] and known that 10^6 kg per year of synthetic organic dyes are dumped into natural environment by the textile factories [4]. Several of synthetic dyes used in different industries and their degradation products are potentially teratogenic, toxic, mutagenic, and carcinogenic [5]. In addition, these dyes not only aesthetically pollute the water due to their color, but also disrupt some biological processes such as the photosynthetic effect, as they also prevent the penetration of sunlight [1]. Thus, the elimination of dyes in wastewater is very essential for ecological balance, animal and human health. Various techniques such as chemical coagulation, flocculation, photodegradation, adsorption, trickling filters, aerobic and anaerobic degradation, oxidation, and membrane separation were proposed to dye removal from wastewater [5,6]. The use of some conventional treatments is difficult in dye removal because of large size, the complex molecular structure, and stability against oxidizing agents, biodegradation and photodegradation of the synthetic dyes [2]. Adsorption is an attractive method for dye removal

due to its easy applicability, low cost for process, high efficiency in removing impurities, and no harmful by-products after the operation [2,7]. Conventional adsorbents used in the adsorption process have some drawbacks such as low removal efficiency due to the lack or scarcity of active sites, high mass transfer resistance because of the bulk structure of adsorbents and difficulty in separation and recovery due to the adsorbent in powder form [8]. Therefore, designing a potential adsorbent that does not have these disadvantages is very important for removing dyes from wastewater both effectively and quickly.

In recent years, magnetic mesoporous silica nanocomposites have been considered as alternative adsorbents for organic dyes and metal ions [9] because of their unique properties such as high specific surface area, tunable pore size and easy separation under external magnetic field [10,11]. In the past decade, various magnetic mesoporous nanocomposites have been used for adsorption of organic dyes and metal ions such as Malachite green [1], Reactive Brilliant Red X-3B [2], Reactive Black 5 [3], Nylosan Blue, Acid Orange 7, Congo Red and Methylene Blue [9], Basic Red 1, and Basic Red 2 [11], Cd(II) [12], Cu(II) [13] and Pb^{2+} [14].

Composed of Fe_3O_4 core and silica shell duo, magnetic nanocomposites have stood out because of their peerless low cytotoxicity, magnetic response, and chemically changeable surface properties. Moreover, if the obtained nanocomposites have superparamagnetism, high magnetization, uniform accessible meso-channels and high surface area, they can be benefit as effective adsorbents to rapidly remove of large contaminants [15]. Especially, great efforts have

[†]To whom correspondence should be addressed.

E-mail: gbeyhan@uludag.edu.tr

Copyright by The Korean Institute of Chemical Engineers.

already been carried out to obtain $\text{Fe}_3\text{O}_4@\text{SiO}_2\text{-R}$ nanocomposite, where R is usually an organic or hybrid organic-silica coating offering N or O-donor sites to coordinate the heavy metal center or active sites to attract the opposite charges electrostatically [13]. In 2004, Wu et al. [16] declared the template assisted synthesis of the magnetic mesoporous particles firstly. According to the synthesis, a silica layer was loaded over the surface of the Fe_3O_4 nanoparticles to prevent the magnetic core from eroding under harsh application conditions. The resulting silica also makes easy to assemble of surfactant template used as structure directing agent. Cationic surfactant molecules and a negatively charged silica surface spontaneously combine on the silica layer to form the framework. The mesoporous silica construction on the magnetite core was created by saturating the spaces around the assembled micellar templates by sol-gel method. After calcination operation to annihilate the surfactant from the silica network, open pores become clear. The silica surface of the mesoporous magnetic nanocomposite particles formed in this way enables various surface functions to be obtained with silanation chemistry that provides "molecular recognition" in many applications. One year later, Zhao et al. [17] obtained particles including hematite core, inner and dense silica shell, and mesoporous outer silica shell in a two-stage process.

The sulphonated azo dyes are one of the most significant groups of synthetic organic dyes and are largely used in the textile and leather industries [3]. Light Green (LG) is a triarylmethane dye and has various detrimental effects such as the potential of permeating and accumulating in the event that skin contact, carcinogenic effects in living system and acting as irritant if inhaled or ingested, the ability to produce sarcomas, lead to methemoglobinemia and, the chronic toxicity [7]. Thus, LG removal from aqueous solutions has been examined utilizing adsorption technique in some studies. The adsorption of LG has been studied using various adsorbents; bottom ash and deoiled soya [7], hexadecylpyridinium bromide (CPB) modified wheat straw [18], $\text{Fe}_3\text{O}_4@\text{SiO}_2@\text{NH}_2$ nanocomposite [19], CPB modified peanut [20], *Salvadora persica* (Miswak) powder [21], CPB modified peanut husk [22], polyethyleneimine-modified carbon nanotubes [23]. However, to the best of our knowledge, $\text{Fe}_3\text{O}_4\text{-CTABSiO}_2\text{-NH}_2$ and $\text{Fe}_3\text{O}_4\text{-SiO}_2\text{-CTABSiO}_2\text{-NH}_2$ for LG removal from aqueous solutions have never been studied.

In our previous paper, $\text{Fe}_3\text{O}_4@\text{SiO}_2@\text{NH}_2$ was produced and used as an adsorbent for LG adsorption [19]. The determined maximum adsorption capacity of $\text{Fe}_3\text{O}_4@\text{SiO}_2@\text{NH}_2$ by using Langmuir isotherm model for the removal of LG was 40.2 mg g^{-1} at 30°C and the natural solution pH. The present adsorption study was executed to investigate the efficiency of the newly prepared mesoporous silica nanocomposites templated with cetyltrimethylammonium bromide (CTAB) and functionalized with amino groups for LG removal from aqueous solutions. CTAB is a cationic surfactant with quaternary ammonium structure and often used to produce various mesoporous silica molecular sieves under basic conditions [24]. Additionally, the -NH_2 groups can be bind to the anionic dye ions by ionic interactions due to their easily protonated property in acidic medium [19]. Therefore, the expectations from this study can be listed as follows: (i) The adsorption capacities of particularly $\text{Fe}_3\text{O}_4\text{-CTABSiO}_2\text{-NH}_2$ and $\text{Fe}_3\text{O}_4\text{-SiO}_2\text{-CTABSiO}_2\text{-NH}_2$ for removal of LG will be higher than that of other ad-

sorbents used for LG removal in the literature, (ii) The superparamagnetism of Fe_3O_4 core will facilitated the separation of the prepared adsorbents from aqueous medium by implementing of an external magnetic field and (iii) The production of the mesoporous silica layer will shorten the process equilibrium time for LG adsorption of the adsorbents by decreasing the mass transfer resistance and multiplying the probability of functionalization. The insight into the role of iron oxide core and porous silica shell in the adsorptive removal of LG can help in refining of the research on nanocomposites [25]. The objective of present study is focused on the synthesis and evaluation of structural, magnetic and adsorption properties of these magnetic silica coated and amino functionalized ($\text{Fe}_3\text{O}_4\text{-SiO}_2\text{-NH}_2$, $\text{Fe}_3\text{O}_4\text{-CTABSiO}_2\text{-NH}_2$ and $\text{Fe}_3\text{O}_4\text{-SiO}_2\text{-CTABSiO}_2\text{-NH}_2$) nanocomposites. Their structural and magnetic features and adsorptive potentials for LG removal were comparatively analyzed. Adsorption isotherms, kinetic and thermodynamic investigations were used for the comparative evaluation of the effect of porous structured shell on the mechanism of adsorption.

MATERIALS AND METHODS

1. Preparation of Adsorbents

Inspired by Massart [26], Fe_3O_4 nanoparticles were synthesized as follows: A mixture of ferrous chloride (10 mL, 2 M, in 2 M HCl) and ferric chloride (40 mL, 1 M) was poured into the ammonia solution (38.5 mL 25% NH_3 plus 500 mL deionized water) infused with nitrogen for 30 min. After being stirred for 30 min under N_2 , the gelatinous precipitate was isolated from the solution with an external magnet without washing with water, since washing the alkaline precipitate with water does not support peptization to obtain stable aqueous sols, which is necessary for successful coating and/or modification. For this purpose, 5% NH_3 solution was used for washing process before drying at 50°C under vacuum.

Silica coating and amino functionalization procedures were adopted from the slightly modified work of Lewandowski et al. [27]. The first adsorbent ($\text{Fe}_3\text{O}_4\text{-SiO}_2\text{-NH}_2$) was obtained as follows: 2 g of magnetite nanoparticles was suspended in 40 mL of a mixture of consisting of ammonia solution, water and 2-propanol (in a 3 : 5 : 65 volume ratio) and then sonicated for 10 min. After being added of Tetraethoxysilane (TEOS), the reaction mixture was sonicated at 40°C for 2 h, and stirred overnight at the same temperature. The as-prepared $\text{Fe}_3\text{O}_4\text{-SiO}_2$ nanoparticles were isolated by magnetic decantation, washed with water and 2-propanol, respectively, and dried at 60°C under vacuum. The second adsorbent ($\text{Fe}_3\text{O}_4\text{-CTABSiO}_2\text{-NH}_2$) was prepared as follows: 0.5 g of magnetite nanoparticles was suspended in a mixture of water, ethyl alcohol and ammonia solution (in a 3 : 8 : 1 mass ratio) and sonicated for 10 min. Then, 0.75 g of CTAB and 4.1 mL of TEOS both diluted with 7.5 mL of ethanol, were simultaneously added, and the mixture was stirred for another 1.5 h. The as-prepared $\text{Fe}_3\text{O}_4\text{-CTABSiO}_2$ nanoparticles were isolated by magnetic decantation, washed with water and ethanol, dried at 60°C under vacuum and calcined at 450°C for 3 h to remove the surfactant. To get the third adsorbent ($\text{Fe}_3\text{O}_4\text{-SiO}_2\text{-CTABSiO}_2\text{-NH}_2$), the processes made for obtaining the first and second adsorbent were combined. That is: the third nanocomposite was prepared as the second nanocomposite

was prepared, with the only difference being that instead of Fe_3O_4 , $\text{Fe}_3\text{O}_4\text{-SiO}_2$ was used as core. For amino functionalization, 0.3 g of $\text{Fe}_3\text{O}_4\text{-SiO}_2$, $\text{Fe}_3\text{O}_4\text{-CTABSiO}_2$, and $\text{Fe}_3\text{O}_4\text{-SiO}_2\text{-CTABSiO}_2$ were suspended in 10 mL of dry toluene and sonicated for 10 min to disperse the particles. Then, 0.63 g of 3-Aminopropyltriethoxysilane (APTES) was added and the mixtures were refluxed for 3 h separately. Finally, the suspensions were isolated by magnetic decantation, washed with toluene and dichloromethane and dried at 35 °C under vacuum. The colors of the nanocomposites were gradually lighter in the order of $\text{Fe}_3\text{O}_4\text{-SiO}_2\text{-NH}_2$, $\text{Fe}_3\text{O}_4\text{-CTABSiO}_2\text{-NH}_2$, and $\text{Fe}_3\text{O}_4\text{-SiO}_2\text{-CTABSiO}_2\text{-NH}_2$.

2. Characterization of Adsorbents

X-ray diffractions of the prepared adsorbents were performed in a Rigaku Ultima-IV X-ray diffractometer. Nanocomposites were scanned in the range of $2\theta=10\text{-}80^\circ$ diffraction angles to determine the phase structure of the nanocomposites. The elemental constituents of the nanocomposites were analyzed with Scanning Electron Microscopy/Energy Dispersed X-ray spectrometer (SEM/EDX, Quanta-Bruker AXS). Magnetic characterizations were realized with Vibrating Sample Magnetometer (VSM, Cryogenic Limited PPMS) with a maximum application area of 20 kOe at room temperature. FT-IR measurements of the samples were realized by using Perkin Elmer-UATR Two series infrared spectrometer. Mesoporosity was investigated with N_2 -adsorption/desorption studies (BET/BJH method) by Quantachrome Autosorb-6 to obtain pore size and pore size distributions. The zeta potentials of $\text{Fe}_3\text{O}_4\text{-SiO}_2\text{-NH}_2$, $\text{Fe}_3\text{O}_4\text{-CTABSiO}_2\text{-NH}_2$ and $\text{Fe}_3\text{O}_4\text{-SiO}_2\text{-CTABSiO}_2\text{-NH}_2$ magnetic adsorbents were measured by Malvern Nano ZS90 to evaluate the pIs of the magnetic adsorbents. The pH value at which the Zeta potential was 0 mV was the pI. All measurements were performed at room temperature. Before the zeta potential measurements, the certain amounts of the magnetic adsorbents were first dispersed by mixing in 50 mL of deionized water until homogeneous suspensions were obtained. The pH values of the suspensions containing the magnetic adsorbents were initially adjusted from 3.0 to 11.0 by using 0.1 M HCl or 0.1 M NaOH. After shaking 5 h, the suspensions were left for 30 min. The samples taken from the supernatants were used to measure the zeta potentials of the magnetic adsorbents by a zeta-sizer.

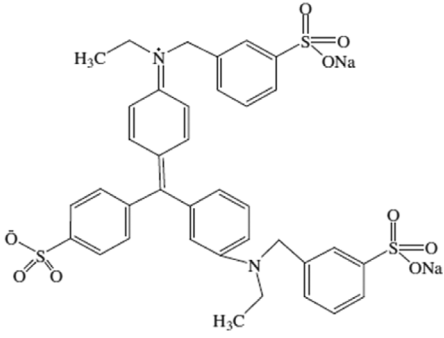
3. Stability of Adsorbents

To test the stability of the adsorbents in acid solution, 5 mg portions of $\text{Fe}_3\text{O}_4\text{-SiO}_2\text{-NH}_2$, $\text{Fe}_3\text{O}_4\text{-CTABSiO}_2\text{-NH}_2$ and $\text{Fe}_3\text{O}_4\text{-SiO}_2\text{-CTABSiO}_2\text{-NH}_2$ were dispersed in 10 mL of 0.01 M HNO_3 solution and shaken for 12 h at room temperature. Afterwards, a magnet was used to separate the adsorbents and solutions. The concentration of Fe in supernatant was measured by Atomic Absorption Spectrophotometer (AAS).

4. Adsorption Studies of Adsorbents

For the adsorption of LG, the effects of chosen parameters such as adsorbent dosage, solution pH, contact time and temperature were tested through batch experiments. LG was procured from BDH Chemicals Ltd and the structure and properties of LG were given in Table 1. In a typical adsorption experiment, 7 mg of $\text{Fe}_3\text{O}_4\text{-SiO}_2\text{-NH}_2$, $\text{Fe}_3\text{O}_4\text{-CTABSiO}_2\text{-NH}_2$ and $\text{Fe}_3\text{O}_4\text{-SiO}_2\text{-CTABSiO}_2\text{-NH}_2$ was homogeneously dispersed in 100 mL of 20 mg L^{-1} LG solution and then agitated by using a magnetic stirrer with temperature con-

Table 1. Chemical structure and properties of Light Green (LG)

Chemical structure	
	
λ_{max} (nm)	: 631
Type	: Anionic
M_w (g mol ⁻¹)	: 792.86
Formula	: $\text{C}_{37}\text{H}_{34}\text{N}_2\text{Na}_2\text{O}_9\text{S}_3$
Azo group	: 1
C.I. Number	: 42095
CAS Number	: 5141-20-8
Solubility	: 200 g L^{-1} (25 °C)

troller at 500 rpm, solution pH (3.48 ± 0.02) and 22 °C temperature until the required adsorption equilibrium conditions. To investigate the parameter effects, temperature, the pH range and adsorbent dosage are 22-32 °C, pH 3-10 and 5-31 mg, respectively. The pH values of the LG solution were adjusted with the aqueous solutions of 0.1 M HCl for low pH values and 0.1 M NaOH for high pH values. The samples drawn with an injector needle by an externally applied magnetic field to the suspension at certain time intervals were analyzed to determine the residual dye amount by using UV-VIS at 631 nm which is maximum absorbance wavelength for LG. For the investigation of LG adsorption kinetics, 7 mg of $\text{Fe}_3\text{O}_4\text{-SiO}_2\text{-NH}_2$, $\text{Fe}_3\text{O}_4\text{-CTABSiO}_2\text{-NH}_2$ and $\text{Fe}_3\text{O}_4\text{-SiO}_2\text{-CTABSiO}_2\text{-NH}_2$ was added into 100 mL of LG solution with the initial solution concentration of 20 mg L^{-1} and then the suspension was stirred at 500 rpm, 22 °C temperature and solution pH (3.48 ± 0.02). The 3 mL of suspension was withdrawn at certain time intervals and the samples were filtered through a syringe filter (0.22 μm of pore size) for determination of the concentration of LG remaining in the suspension. Adsorption isotherm experiments were implemented with 100 mL of 20 mg L^{-1} LG solution at solution pH (3.48 ± 0.02) and 22 °C temperature for 30 min after the addition of 7 mg of adsorbents.

In the adsorption process, the percent of removal efficiency (R%) was obtained by using Eq. (1) and the adsorption capacity (q_e) was calculated with Eq. (2):

$$R\% = \frac{(C_0 - C_e)}{C_0} \times 100 \quad (1)$$

$$q_e = \frac{(C_0 - C_e)V}{m} \quad (2)$$

where C_0 and C_e are ascribed to the initial and equilibrium concentrations for LG solution (mg L^{-1}); m indicates the mass of the adsorbents (g); and V indicates the volume (L) of LG solution.

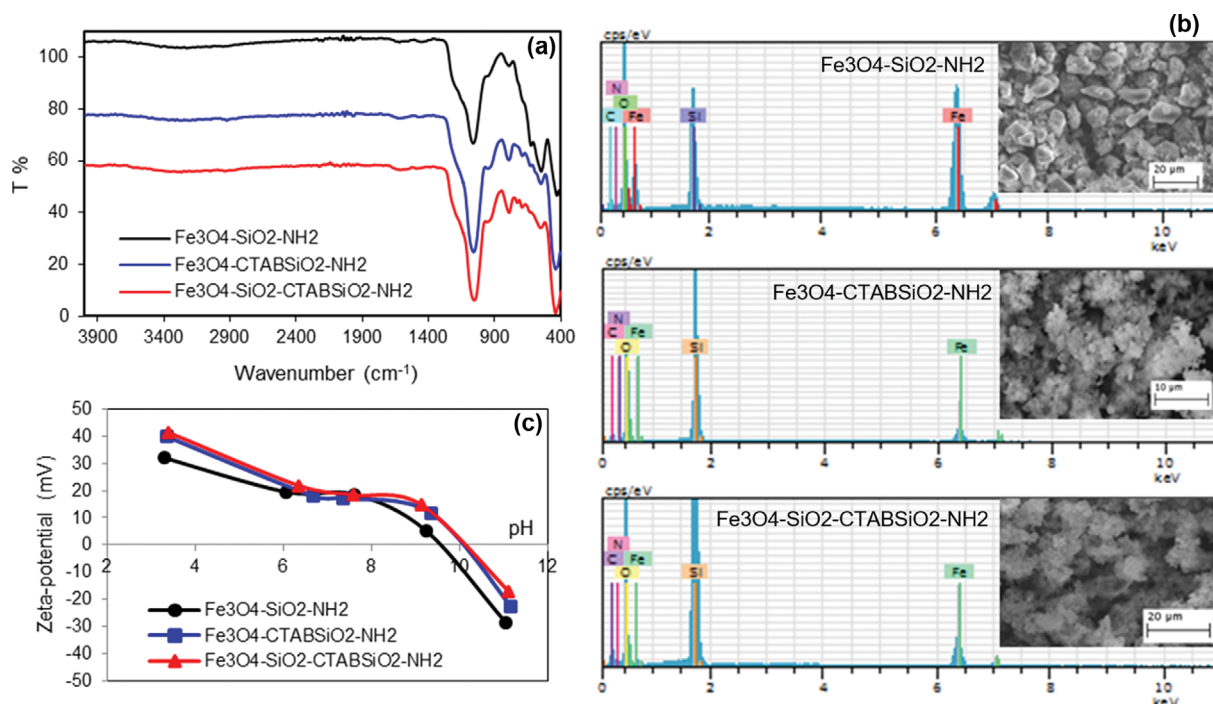


Fig. 1. (a) FTIR spectra, (b) SEM images and EDX, (c) zeta potential measurements of $\text{Fe}_3\text{O}_4\text{-SiO}_2\text{-NH}_2$, $\text{Fe}_3\text{O}_4\text{-CTABSiO}_2\text{-NH}_2$ and $\text{Fe}_3\text{O}_4\text{-SiO}_2\text{-CTABSiO}_2\text{-NH}_2$ nanocomposites.

RESULTS AND DISCUSSION

1. Characterization Results

FT-IR spectra for $\text{Fe}_3\text{O}_4\text{-SiO}_2\text{-NH}_2$, $\text{Fe}_3\text{O}_4\text{-CTABSiO}_2\text{-NH}_2$ and $\text{Fe}_3\text{O}_4\text{-SiO}_2\text{-CTABSiO}_2\text{-NH}_2$ are shown in Fig. 1(a). Essentially, our expectation is that FT-IR spectra are very similar for all samples, except for some details. That is; all samples show the characteristic absorption of Fe-O vibration band at 560 cm^{-1} . Also, the bending and stretching of O-H bands around $1,640$ and $3,400\text{ cm}^{-1}$, associated with the adsorbed water molecules, were seen in all samples. The absorption bands which exist for all samples at about 809 and $1,076\text{ cm}^{-1}$ are relevant to the symmetric and asymmetric stretching of Si-O-Si bonds [28]. Albeit it is valid for three samples, the bending vibration bands of Si-O-Si and Si-OH which are observed at 439 and 965 cm^{-1} are more intensive for $\text{Fe}_3\text{O}_4\text{-CTABSiO}_2\text{-NH}_2$ and $\text{Fe}_3\text{O}_4\text{-SiO}_2\text{-CTABSiO}_2\text{-NH}_2$ samples in comparison with $\text{Fe}_3\text{O}_4\text{-SiO}_2\text{-NH}_2$. Because these bands are indicative for the density of the silica layer on Fe_3O_4 nanoparticles [29], on the contrary, for $\text{Fe}_3\text{O}_4\text{-SiO}_2\text{-NH}_2$ sample Fe-O vibration peak is the most intensive among the samples, which confirms the shifting of Fe-O vibration absorption to Fe-O-Si vibration absorption (584 cm^{-1}) [30]. Also, the absorption bands attributed to the bands of the amino groups at $3,361$, $1,575$, $1,475$ and 692 cm^{-1} [31] exist for all samples, which indicate the successful amino functionalization. Even if small absorption peaks appeared around $2,800\text{-}3,000\text{ cm}^{-1}$ indicating the vibrations of $-\text{CH}_2$ of CTAB templates in the $\text{Fe}_3\text{O}_4\text{-CTABSiO}_2\text{-NH}_2$ and $\text{Fe}_3\text{O}_4\text{-SiO}_2\text{-CTABSiO}_2\text{-NH}_2$ samples, there are not salient peaks suggesting the substantial removal of CTAB from the pores [32].

According to the SEM/EDX results (Fig. 1(b)), we can see that all samples contain Fe, O, Si, C, and N elements the distributions

of which changes from one sample to another. This graphic confirms the successful Fe_3O_4 synthesis, silica covering and amino functionalization, respectively. The SEM images displayed in insets of Fig. 1(b) show that $\text{Fe}_3\text{O}_4\text{-SiO}_2\text{-NH}_2$ sample seems to be aggregated due to dipole-dipole interaction, while the $\text{Fe}_3\text{O}_4\text{-CTABSiO}_2\text{-NH}_2$ and $\text{Fe}_3\text{O}_4\text{-SiO}_2\text{-CTABSiO}_2\text{-NH}_2$ samples look good dispersal due to the repulsion of magnetic nanoparticles [33]. The coating with silica layer resulted in separation of the particles by sterically and electrostatically, thereby reducing aggregation. Although the electrostatic repulsion changes depending on the ionic strength and solution pH, steric repulsion mainly depends upon the density of inorganic silica polymer [34].

The correlation between the zeta potential and pH values provides convenience in determining the subsequent process conditions to obtain optimum adsorption data and characterizing the stability of the dispersion. For example, positive or negative high zeta potential values indicate stable systems and we can get the pI value, which means the pH value at which the zeta potential of functional nanoparticles is equal to zero. Electrostatic repulsion between the charged nanoparticles increases dispersibility and also the stability of particles [31,35]. The results of the zeta potential analysis of the $\text{Fe}_3\text{O}_4\text{-SiO}_2\text{-NH}_2$, $\text{Fe}_3\text{O}_4\text{-CTABSiO}_2\text{-NH}_2$ and $\text{Fe}_3\text{O}_4\text{-SiO}_2\text{-CTABSiO}_2\text{-NH}_2$ nanocomposites at varied pH are shown in Fig. 1(c). It can be concluded from the results, the isoelectric points of $\text{Fe}_3\text{O}_4\text{-SiO}_2\text{-NH}_2$, $\text{Fe}_3\text{O}_4\text{-CTABSiO}_2\text{-NH}_2$ and $\text{Fe}_3\text{O}_4\text{-SiO}_2\text{-CTABSiO}_2\text{-NH}_2$ were found at 9.57 , 10.09 and 10.13 , respectively. These high values show that the surface of all nanocomposites is positively charged at pH values under about 10.00 , which is proper for the anionic pollutant's adsorption [28]. Compared with $\text{Fe}_3\text{O}_4\text{-SiO}_2\text{-NH}_2$, $\text{Fe}_3\text{O}_4\text{-CTABSiO}_2\text{-NH}_2$ and $\text{Fe}_3\text{O}_4\text{-SiO}_2\text{-CTABSiO}_2\text{-NH}_2$ have a

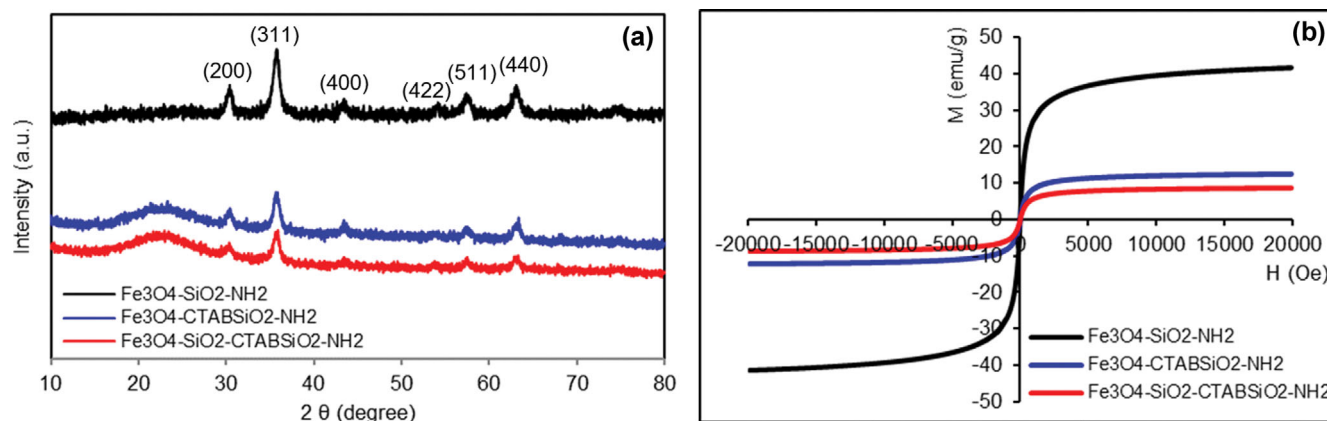


Fig. 2. (a) XRD patterns and (b) magnetization curves of $\text{Fe}_3\text{O}_4\text{-SiO}_2\text{-NH}_2$, $\text{Fe}_3\text{O}_4\text{-CTABSiO}_2\text{-NH}_2$ and $\text{Fe}_3\text{O}_4\text{-SiO}_2\text{-CTABSiO}_2\text{-NH}_2$ nanocomposites.

higher isoelectric point which may be due to the more electron donor moieties, which causes the increased the surface charge on the $\text{Fe}_3\text{O}_4\text{-CTABSiO}_2\text{-NH}_2$ and $\text{Fe}_3\text{O}_4\text{-SiO}_2\text{-CTABSiO}_2\text{-NH}_2$ samples [36]. Due to the stronger ability of combining H^+ , $\text{Fe}_3\text{O}_4\text{-CTABSiO}_2\text{-NH}_2$ and $\text{Fe}_3\text{O}_4\text{-SiO}_2\text{-CTABSiO}_2\text{-NH}_2$ samples had a higher pI than $\text{Fe}_3\text{O}_4\text{-SiO}_2\text{-NH}_2$ nanocomposite.

The structures of the magnetic nanocomposites silica encapsulated and amino functionalized were qualified by XRD (Fig. 2(a)) to characterize the samples with respect to phase structures. As shown in Fig. 2(a), all the peak positions at 30.4° (200), 35.7° (311), 43.4° (400), 53.6° (422), 57.3° (511) and 62.9° (440) were coherent with the standard X-ray data for Fe_3O_4 magnetite phase. This is evidence of the inverse spinel structure of Fe_3O_4 and shows that the magnetite continues to exist after being coated with silica. As the coating process develops, the peak intensity of Fe_3O_4 has decreased, which was ascribed to the silica shell wrapped on the particles surface, while there was an increasing order of amorphous silica (at around $2\theta=20^\circ$), which represents the increased silica layer thickness [31,35].

High saturation magnetization (M_s), mainly depends on the chemical composition of magnetic nanoparticles, and no coercivity together with remanent magnetization are important indicators of emerging superparamagnetic properties [37]. Fig. 2(b) refers to the superparamagnetic character of $\text{Fe}_3\text{O}_4\text{-SiO}_2\text{-NH}_2$, $\text{Fe}_3\text{O}_4\text{-CTABSiO}_2\text{-NH}_2$ and $\text{Fe}_3\text{O}_4\text{-SiO}_2\text{-CTABSiO}_2\text{-NH}_2$ nanocomposites because of having zero coercivity and no remanence. The saturation magnetizations of $\text{Fe}_3\text{O}_4\text{-SiO}_2\text{-NH}_2$, $\text{Fe}_3\text{O}_4\text{-CTABSiO}_2\text{-NH}_2$ and $\text{Fe}_3\text{O}_4\text{-SiO}_2\text{-CTABSiO}_2\text{-NH}_2$ are 41.7, 12.5 and 8.8 emu g^{-1} respectively. In comparison to $\text{Fe}_3\text{O}_4\text{-SiO}_2\text{-NH}_2$, the decreased saturation magnetization of the last two nanocomposites is mainly resulted in the insulating effect of silica shells. The progressive thickening of the silica layer caused to the decrease of M_s [31].

The N_2 -sorption isotherms have been used to obtain information about the mesoporosity of the materials. The isotherms and the pore-size distributions of the nanocomposites are given in Fig. 3(a), (b). According to IUPAC classification, all of the samples exhibited type IV isotherm with different types of hysteresis loops, thereby indicating the mesoporosity of the materials. Because hysteresis appearing in the multilayer range of physisorption isotherms

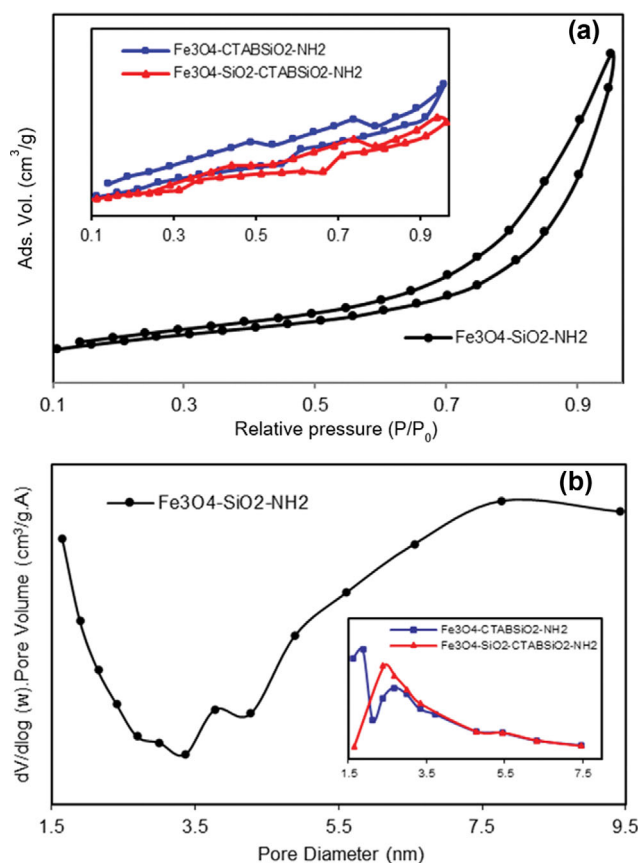


Fig. 3. (a) N_2 -adsorption/desorption isotherms and (b) pore size distributions of $\text{Fe}_3\text{O}_4\text{-SiO}_2\text{-NH}_2$, $\text{Fe}_3\text{O}_4\text{-CTABSiO}_2\text{-NH}_2$ and $\text{Fe}_3\text{O}_4\text{-SiO}_2\text{-CTABSiO}_2\text{-NH}_2$ nanocomposites.

is usually associated with capillary condensation in mesopore structure [38]. For the $\text{Fe}_3\text{O}_4\text{-CTABSiO}_2\text{-NH}_2$ and $\text{Fe}_3\text{O}_4\text{-SiO}_2\text{-CTABSiO}_2\text{-NH}_2$ samples, the H2-type hysteresis loops at relative pressure (p/p_0) between 0.4 and 1.0 implied their regular and mesoporous structures (inset of Fig. 3(a)) and this type of loop can be attributed to pore-blocking/percolation in a narrow range of pore necks. $\text{Fe}_3\text{O}_4\text{-SiO}_2\text{-NH}_2$ showed H3-type hysteresis loop at p/p_0 between

0.8 and 1.0. This loop is a typical characteristic of mesoporous materials because of the aggregation of the primary nanoparticles [8]. Isotherms that reveal the H3 type do not exhibit any restrictive adsorption at the high p/p_0 obtained in non-rigid aggregates consisting of plate-like particles, as in $\text{Fe}_3\text{O}_4\text{-SiO}_2\text{-NH}_2$ [39]. The BJH pore-size distribution (Fig. 3(b)) curves showed that only $\text{Fe}_3\text{O}_4\text{-SiO}_2\text{-CTABSiO}_2\text{-NH}_2$ sample (inset of Fig. 3(b)) exhibited uniform pore size with a diameter of 2.4 nm. For $\text{Fe}_3\text{O}_4\text{-CTABSiO}_2\text{-NH}_2$ sample (inset of Fig. 3(b)), 1.9 and 2.4 nm, which has a bimodal distribution, for $\text{Fe}_3\text{O}_4\text{-SiO}_2\text{-NH}_2$ sample broad pore distribution was obtained. The large pores for $\text{Fe}_3\text{O}_4\text{-SiO}_2\text{-NH}_2$ samples centered around 7.8 nm were produced by the aggregation of the primary nanoparticles. Of porous materials, amorphous ones exhibit a wide pore size distribution predominantly on the mesopore scale, which restricts the shape selectivity and effectiveness of the materials [39].

2. Adsorption Results

2-1. Effect of Adsorbent Dosage

The effect of $\text{Fe}_3\text{O}_4\text{-SiO}_2\text{-CTABSiO}_2\text{-NH}_2$ amount on the removal of LG was studied for adsorbent amount varying from 5 to 31 mg in 100 mL of a 20 mg L^{-1} concentration of LG solution. As can be seen from the Fig. 4, an increase in dosage of $\text{Fe}_3\text{O}_4\text{-SiO}_2\text{-CTABSiO}_2\text{-NH}_2$ causes an increase in R% of LG and after a dosage of 10.9 mg for the adsorbent, the removal percentage becomes constant as the dosage of adsorbent increases. This observation is due to the enhancement in the surface area of $\text{Fe}_3\text{O}_4\text{-SiO}_2\text{-CTABSiO}_2\text{-NH}_2$ as well as the high availability of adsorption sites that have become more accessible [19]. The LG adsorption capacity of $\text{Fe}_3\text{O}_4\text{-SiO}_2\text{-CTABSiO}_2\text{-NH}_2$ increased up to the adsorbent dose of 7.3 mg and then decreased sharply with increasing the dosage of nanocomposite. The reason for this result is the tendency to agglomerate of the nanocomposite particles in the aqueous phase with the increase in adsorbent dosage, and thus a lowering in the surface area of $\text{Fe}_3\text{O}_4\text{-SiO}_2\text{-CTABSiO}_2\text{-NH}_2$ [24]. Hence, the dosage of $\text{Fe}_3\text{O}_4\text{-SiO}_2\text{-CTABSiO}_2\text{-NH}_2$ was selected to be 7 mg/100 mL for LG adsorption considering the contact time, the adsorption capacity and the removal percentage. In the present study, in order to compare the adsorption capacities of the adsorbents, optimum

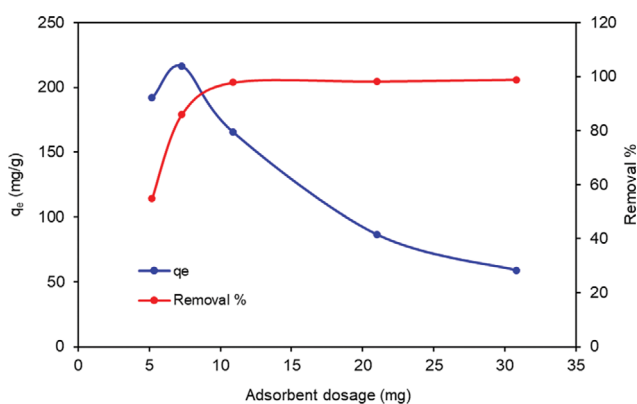


Fig. 4. Effect of adsorbent dosage on LG adsorption with $\text{Fe}_3\text{O}_4\text{-SiO}_2\text{-CTABSiO}_2\text{-NH}_2$ (initial concentration: 20 mg/L, solution volume: 100 mL, agitation rate: 500 rpm, temperature: 22 °C, pH: (3.48±0.02)).

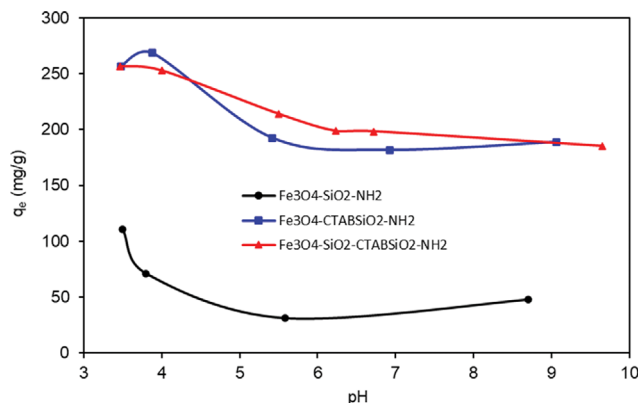


Fig. 5. Effect of pH on LG adsorption with $\text{Fe}_3\text{O}_4\text{-SiO}_2\text{-NH}_2$, $\text{Fe}_3\text{O}_4\text{-CTABSiO}_2\text{-NH}_2$ and $\text{Fe}_3\text{O}_4\text{-SiO}_2\text{-CTABSiO}_2\text{-NH}_2$ (initial concentration: 20 mg/L, solution volume: 100 mL, agitation rate: 500 rpm, adsorbent dosage: 7 mg, temperature: 22 °C).

adsorbent dosages of $\text{Fe}_3\text{O}_4\text{-SiO}_2\text{-NH}_2$ and $\text{Fe}_3\text{O}_4\text{-CTABSiO}_2\text{-NH}_2$ were also chosen as 7 mg/100 mL.

2-2. Effect of pH

Changes in the initial pH of dye solution in adsorption system is crucial due to their effects on the change of the adsorbent surface charge by protonation or deprotonation of various functional groups on the surface and also on the ionization and speciation of dye molecules in solution [2]. The effect of initial solution pH on LG adsorption with $\text{Fe}_3\text{O}_4\text{-SiO}_2\text{-NH}_2$, $\text{Fe}_3\text{O}_4\text{-CTABSiO}_2\text{-NH}_2$ and $\text{Fe}_3\text{O}_4\text{-SiO}_2\text{-CTABSiO}_2\text{-NH}_2$ were shown in Fig. 5. As shown in Fig. 5, if the initial pH of LG solution changes from 3 to 10, the adsorption capacities of $\text{Fe}_3\text{O}_4\text{-SiO}_2\text{-NH}_2$, $\text{Fe}_3\text{O}_4\text{-CTABSiO}_2\text{-NH}_2$ and $\text{Fe}_3\text{O}_4\text{-SiO}_2\text{-CTABSiO}_2\text{-NH}_2$ decrease from 110.56, 256.91 and 256.79 to 47.78, 188.87 and 185.24 mg g^{-1} , respectively. According to the zeta potential analysis, the surfaces of $\text{Fe}_3\text{O}_4\text{-SiO}_2\text{-NH}_2$ (pI=9.57), $\text{Fe}_3\text{O}_4\text{-CTABSiO}_2\text{-NH}_2$ (pI=10.09) and $\text{Fe}_3\text{O}_4\text{-SiO}_2\text{-CTABSiO}_2\text{-NH}_2$ (pI=10.13) are positively charged due to protonated of NH_2 groups at pH lower than the pI. In this case, the reason for the adsorption of LG ions is the electrostatic interaction of the anionic dye with the positively charged surfaces of $\text{Fe}_3\text{O}_4\text{-SiO}_2\text{-NH}_2$, $\text{Fe}_3\text{O}_4\text{-CTABSiO}_2\text{-NH}_2$ and $\text{Fe}_3\text{O}_4\text{-SiO}_2\text{-CTABSiO}_2\text{-NH}_2$ in $\text{pH} < \text{pI}$. When the initial solution pH increases, the amount of dye adsorbed decreases since the zeta potential values of the adsorbents become less positive. However, different from this general observation, it was determined that the adsorption of LG increased at pH 8.70 for $\text{Fe}_3\text{O}_4\text{-SiO}_2\text{-NH}_2$ and pH 9.06 for $\text{Fe}_3\text{O}_4\text{-CTABSiO}_2\text{-NH}_2$. This result can be explained by considering different types of interactions between $\text{Fe}_3\text{O}_4\text{-SiO}_2\text{-NH}_2$ and $\text{Fe}_3\text{O}_4\text{-CTABSiO}_2\text{-NH}_2$ with LG in this case [22].

2-3. Effect of Contact Time and Adsorption Kinetics

The role of contact time, one of the critical parameters affecting the adsorption efficiency, was tested for LG adsorption onto $\text{Fe}_3\text{O}_4\text{-SiO}_2\text{-NH}_2$, $\text{Fe}_3\text{O}_4\text{-CTABSiO}_2\text{-NH}_2$ and $\text{Fe}_3\text{O}_4\text{-SiO}_2\text{-CTABSiO}_2\text{-NH}_2$ in the range of 0-120 min at solution pH (3.48±0.02). As can be seen from Fig. 6(a) that the rate of LG adsorption was fairly fast in the first stage for the adsorption during the first 15 min for $\text{Fe}_3\text{O}_4\text{-CTABSiO}_2\text{-NH}_2$ and $\text{Fe}_3\text{O}_4\text{-SiO}_2\text{-CTABSiO}_2\text{-NH}_2$ and

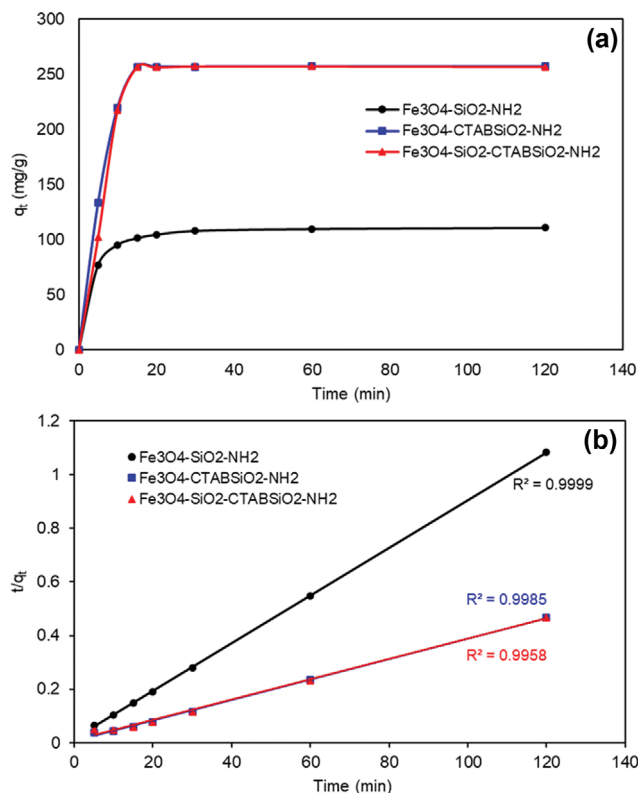


Fig. 6. (a) Effect of contact time and (b) plot of time versus t/q_t for LG adsorption on $Fe_3O_4-SiO_2-NH_2$, $Fe_3O_4-CTABSiO_2-NH_2$ and $Fe_3O_4-SiO_2-CTABSiO_2-NH_2$ (initial concentration: 20 mg L^{-1} , solution volume: 100 mL, agitation rate: 500 rpm, adsorbent dosage: 7 mg, temperature: 22°C , pH: (3.48 ± 0.02)).

the first 5 min for $Fe_3O_4-SiO_2-NH_2$ thanks to the intensive interactions between LG molecules and nanocomposites due to the effect of the unoccupied adsorption sites of the adsorbents [2]. After the initial stages, LG adsorption rate decreases slowly and then the adsorption capacity attains to equilibrium at 30 min for $Fe_3O_4-SiO_2-NH_2$ whereas the adsorption of dye rapidly reaches equilibrium at 15 min for $Fe_3O_4-CTABSiO_2-NH_2$ and $Fe_3O_4-SiO_2-CTABSiO_2-NH_2$ because of higher content of amino group grafted onto the mesoporous sites. In addition, according to this result, thanks to the mesoporous structure of $Fe_3O_4-CTABSiO_2-NH_2$ and $Fe_3O_4-SiO_2-$

$CTABSiO_2-NH_2$ prepared in this study, the availability of the active sites of the adsorbents by LG molecules was increased and the mass transfer resistance that occurs in the adsorption process was also effectively reduced [8]. The short equilibrium time shows the advantage of using $Fe_3O_4-CTABSiO_2-NH_2$ and $Fe_3O_4-SiO_2-CTABSiO_2-NH_2$ in LG removal from wastewaters.

The kinetic adsorption data, which were determined experimentally, were fitted to two common kinetic models for the purpose of explain the rate controller step for the mechanism of the adsorption, the main parameters presiding the characteristics and kinetics of adsorption. The linearized forms of pseudo first order and pseudo second order kinetic models extensively applied to define dye adsorption on adsorbents are given in Eqs. (3) and (4), respectively [21]:

$$\ln(q_e - q_t) = \ln q_e - k_1 t \quad (3)$$

$$\frac{t}{q_t} = \frac{1}{k_2 q_e^2} + \frac{t}{q_e} \quad (4)$$

where k_1 and k_2 refer to the first and the second order rate constants, respectively. These rate constants are determined by the slopes of the plots $\ln(q_e - q_t)$ and t/q_t versus t , respectively. The rate constants (k_1 and k_2), the experimental adsorption capacity ($q_{e,exp}$), the correlation coefficients (R^2) and the calculated adsorption capacities ($q_{e,cal}$) are given in Table 2.

The results clearly indicate that the pseudo second order kinetic model was fitted well with the experimental adsorption data (Fig. 6(b)) since its R^2 value was higher than that of the pseudo first order model. Additionally, $q_{e,cal}$ determined from the equation of the pseudo-second-order model was very close to $q_{e,exp}$ determined from the experiments. According to these results, the appropriate model to define the adsorption kinetics of LG adsorption on $Fe_3O_4-SiO_2-NH_2$, $Fe_3O_4-CTABSiO_2-NH_2$ and $Fe_3O_4-SiO_2-CTABSiO_2-NH_2$ is the second-order. Additionally, LG adsorption process was probably predominated with a chemical adsorption phenomenon. The chemical adsorption could be a rate controlling step in this study and the adsorption process occurs through chemical interactions rather than physical forces [2,40,41]. In previously conducted studies, the conformity of the pseudo second order model for LG adsorption on various adsorbents was reported [7,19,21,23].

2-4. Adsorption Isotherms

In an adsorption study, adsorption isotherms are very practical

Table 2. Kinetic results of pseudo first order and pseudo second order for the adsorption of LG onto $Fe_3O_4-SiO_2-NH_2$, $Fe_3O_4-CTABSiO_2-NH_2$ and $Fe_3O_4-SiO_2-CTABSiO_2-NH_2$ nanocomposites

Kinetic model	Kinetic parameters	Adsorbents		
		$Fe_3O_4-SiO_2-CTABSiO_2-NH_2$	$Fe_3O_4-CTABSiO_2-NH_2$	$Fe_3O_4-SiO_2-NH_2$
Pseudo-first-order	$q_{e,exp}$ (mg g^{-1})	256.79	256.91	110.56
	k_1 (min^{-1})	0.37	0.28	0.07
	$q_{e,cal}$ (mg g^{-1})	495.71	251.24	40.96
	R^2	0.8620	0.8778	0.8529
Pseudo-second-order	k_2 ($\text{g mg}^{-1} \text{min}^{-1}$)	1.52×10^{-3}	2.89×10^{-3}	5.21×10^{-3}
	$q_{e,cal}$ (mg g^{-1})	263.16	263.16	112.36
	R^2	0.9958	0.9985	0.9999

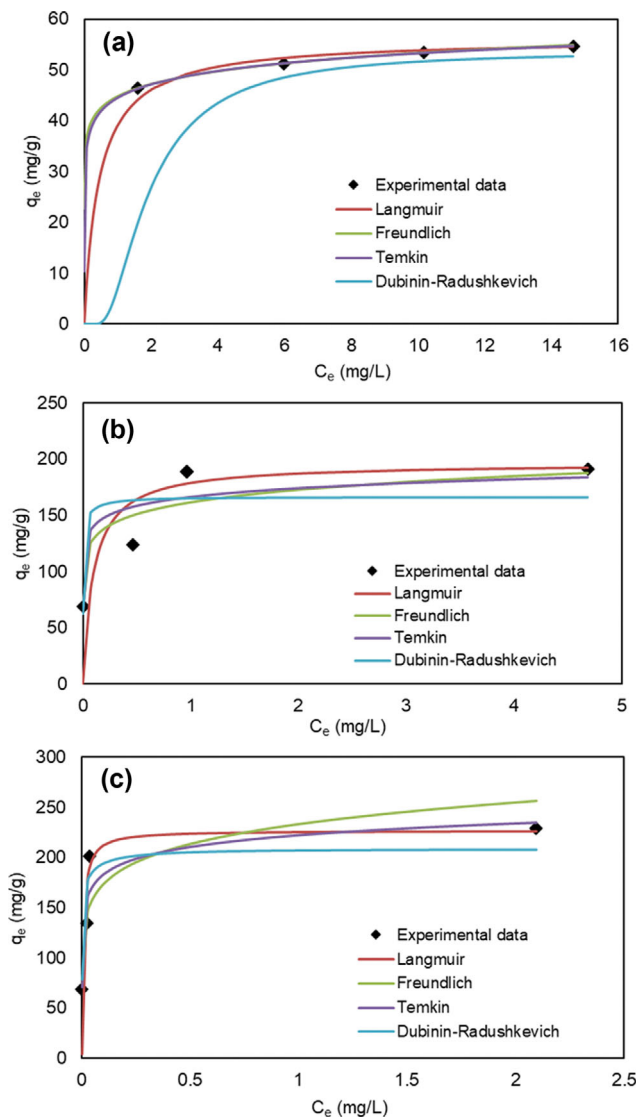


Fig. 7. Isotherms plots for the adsorption of LG onto (a) $\text{Fe}_3\text{O}_4\text{-SiO}_2\text{-NH}_2$, (b) $\text{Fe}_3\text{O}_4\text{-CTABSiO}_2\text{-NH}_2$ and (c) $\text{Fe}_3\text{O}_4\text{-SiO}_2\text{-CTABSiO}_2\text{-NH}_2$.

to explain the adsorption mechanisms, the relation between the amount of adsorbed dye per unit mass of adsorbent (q_e , mg g^{-1}) at a given temperature under equilibrium conditions and the dye concentration in the liquid phase (C_e , mg L^{-1}) and affinity of an adsorbent for a dye and surface properties [1]. The range of solution initial concentration was chosen as 5–20 mg L^{-1} for the isotherm study. The adsorption isotherms for LG adsorption on $\text{Fe}_3\text{O}_4\text{-SiO}_2\text{-NH}_2$, $\text{Fe}_3\text{O}_4\text{-CTABSiO}_2\text{-NH}_2$ and $\text{Fe}_3\text{O}_4\text{-SiO}_2\text{-CTABSiO}_2\text{-NH}_2$ were demonstrated in Fig. 7(a)–(c). As can be seen from Fig. 7(a)–(c) that, when the equilibrium concentrations of LG, C_e (mg L^{-1}), increases, the equilibrium adsorption capacities, q_e (mg g^{-1}), increases. This result showed that the adsorbents possess high affinity and very strong adsorption ability for LG [2].

The adsorption isotherms for LG adsorption on $\text{Fe}_3\text{O}_4\text{-SiO}_2\text{-NH}_2$, $\text{Fe}_3\text{O}_4\text{-CTABSiO}_2\text{-NH}_2$ and $\text{Fe}_3\text{O}_4\text{-SiO}_2\text{-CTABSiO}_2\text{-NH}_2$ were carried out at 22 °C. In determine to the adsorption mechanism, the equilibrium data which were obtained from adsorption experiments

were tested by Langmuir, Freundlich, Temkin and Dubinin-Radushkevich isotherm models and these mentioned models can be expressed by the following equations, respectively [18,21,24]:

$$\frac{C_e}{q_e} = \frac{1}{K_L q_{e, \max}} + \frac{C_e}{q_{e, \max}} \quad (5)$$

$$\ln q_e = \ln K_F + \frac{1}{n} \ln C_e \quad (6)$$

$$q_e = B_T \ln(K_T) + B_T \ln(C_e) \quad (7)$$

$$\ln q_e = \ln q_{e, \max} - K_{D-R} \left[RT \ln \left(1 + \frac{1}{C_e} \right) \right]^2 \quad (8)$$

where $q_{e, \max}$ (mg g^{-1}) is the maximum adsorption capacity of LG, q_e (mg g^{-1}) is the amount of adsorbed onto the adsorbents at equilibrium conditions, C_e is the LG equilibrium concentration (mg L^{-1}), K_L (L mg^{-1}), K_F ($(\text{mg g}^{-1}) (\text{L mg}^{-1})^{1/n}$), K_T (L mg^{-1}) and K_{D-R} ($\text{mol}^2 \text{J}^{-2}$) are the Langmuir, the Freundlich, the Temkin and the Dubinin-Radushkevich constants, respectively. n is the Freundlich constant, and B_T (J mol^{-1}) is a constant relevant to the heat of adsorption.

The correlation coefficients determined for the isotherm models and the calculated isotherm parameters were given in Table 3. Depending on the R^2 values given in Table 3, the experimental results of the adsorption process showed the best fit to the Langmuir isotherm among all isotherm models. The result implies that LG adsorption onto $\text{Fe}_3\text{O}_4\text{-SiO}_2\text{-NH}_2$, $\text{Fe}_3\text{O}_4\text{-CTABSiO}_2\text{-NH}_2$ and $\text{Fe}_3\text{O}_4\text{-SiO}_2\text{-CTABSiO}_2\text{-NH}_2$ follows monolayer adsorption (chemisorption) on energetically uniform adsorbent surface [2]. Similar results to those obtained in this study for testing the adsorption isotherm were reported in the literature for LG adsorption [18,19, 22]. It was shown from Table 3, the maximum adsorption capacities of $\text{Fe}_3\text{O}_4\text{-SiO}_2\text{-NH}_2$, $\text{Fe}_3\text{O}_4\text{-CTABSiO}_2\text{-NH}_2$ and $\text{Fe}_3\text{O}_4\text{-SiO}_2\text{-CTABSiO}_2\text{-NH}_2$ for LG are 56.18, 196.08 and 227.27 mg g^{-1} , respectively. $q_{e, \max}$ values for LG adsorption with $\text{Fe}_3\text{O}_4\text{-CTABSiO}_2\text{-NH}_2$ and $\text{Fe}_3\text{O}_4\text{-SiO}_2\text{-CTABSiO}_2\text{-NH}_2$ were found to be larger than that with $\text{Fe}_3\text{O}_4\text{-SiO}_2\text{-NH}_2$. The higher LG adsorption capacities observed for $\text{Fe}_3\text{O}_4\text{-CTABSiO}_2\text{-NH}_2$ and $\text{Fe}_3\text{O}_4\text{-SiO}_2\text{-CTABSiO}_2\text{-NH}_2$ can be ascribed to higher porosity of the adsorbents and the different binding strength between LG and amine groups on the surfaces of the adsorbents [4]. The n values obtained by the Freundlich isotherm model for all adsorbents were larger than unity ($n > 1$). This observation indicated that the interaction forces between LG and the adsorbents are strong and confirm favorable adsorption process for synthesized nanocomposites [1,22].

The Dubinin-Radushkevich isotherm model was implemented to the adsorption equilibrium data to determine whether the adsorption of LG onto the $\text{Fe}_3\text{O}_4\text{-SiO}_2\text{-NH}_2$, $\text{Fe}_3\text{O}_4\text{-CTABSiO}_2\text{-NH}_2$ and $\text{Fe}_3\text{O}_4\text{-SiO}_2\text{-CTABSiO}_2\text{-NH}_2$ is inherently physical or chemical. The sorption energy, E can be calculated from K_{D-R} provides information about the mechanism of adsorption as chemical ion exchange or physical [21]:

$$E = \frac{1}{\sqrt{2K_{D-R}}} \quad (9)$$

The E values calculated by using Eq. (9) are given in Table 3. According to the Table 3, the chemical ion exchange is dominant in

Table 3. Parameters of adsorption models for the adsorption of LG onto Fe₃O₄-SiO₂-NH₂, Fe₃O₄-CTABSiO₂-NH₂ and Fe₃O₄-SiO₂-CTAB-SiO₂-NH₂ nanocomposites

Isotherm model	Isotherm parameters	Adsorbents		
		Fe ₃ O ₄ -SiO ₂ -CTABSiO ₂ -NH ₂	Fe ₃ O ₄ -CTABSiO ₂ -NH ₂	Fe ₃ O ₄ -SiO ₂ -NH ₂
Langmuir	q _{max} (mg g ⁻¹)	227.27	196.08	56.18
	K _L (L mg ⁻¹)	146.67	10.20	2.28
	R ²	0.9999	0.9969	0.9996
Freundlich	n	7.82	10.29	13.19
	K _F (mg ^{1-1/n} L ^{1/n} g ⁻¹)	233.41	161.37	44.74
	R ²	0.8872	0.9104	0.9992
Temkin	B _T	16.85	11.29	3.81
	K _T (L mg ⁻¹)	5.37×10 ⁵	2.43×10 ⁶	1.20×10 ⁵
	R ²	0.8771	0.8322	0.9992
Dubinin-Radushkevich	q _{max} (mg g ⁻¹)	207.97	165.65	53.57
	K _{D-R} (mol ² J ⁻²)	2×10 ⁻⁹	2×10 ⁻⁹	1×10 ⁻⁷
	R ²	0.9033	0.8338	0.9078
	E (kJ mol ⁻¹)	15.81	15.81	2.24

Table 4. Comparison of the adsorption capacities determined from Langmuir isotherm of various adsorbents for the adsorption of LG

Adsorbents	Max. adsorption capacities (mg g ⁻¹)	Refs.
Bottom ash	8.40	[7]
Deoiled soya	7.29	[7]
CPB modified wheat straw	70.01	[18]
CPB modified peanut	60.5	[20]
Salvadora persica (Miswak) powder	252.0	[21]
CPB modified peanut husk	146.2	[22]
Kohlrabi peel	36.1	[22]
Rice husk	32.6	[22]
PEI-modified carbon nanotubes	469	[23]
Fe ₃ O ₄ -SiO ₂ -NH ₂	56.18	In this study
Fe ₃ O ₄ -CTABSiO ₂ -NH ₂	196.08	In this study
Fe ₃ O ₄ -SiO ₂ -CTABSiO ₂ -NH ₂	227.27	In this study

the adsorption of LG onto the adsorbents except Fe₃O₄-SiO₂-NH₂ since the E values were determined between 8 and 16 kJ mol⁻¹, and these values refer the role of chemisorption in the adsorption [7].

The adsorption performances of Fe₃O₄-SiO₂-NH₂, Fe₃O₄-CTAB-SiO₂-NH₂ and Fe₃O₄-SiO₂-CTABSiO₂-NH₂ were compared with the various adsorbents preferred in previous studies for LG adsorption. The comparing of the maximum adsorption capacities estimated by using Langmuir isotherm model for LG adsorption of different adsorbents was given in Table 4.

According to the results given in Table 4, the adsorption capacities determined from Langmuir isotherm of the adsorbents prepared in this study are comparable or higher than the adsorption capacities of other adsorbents previously used for LG adsorption. The adsorption capacity of Fe₃O₄-SiO₂-NH₂ determined by using Langmuir isotherm model for LG adsorption is very similar to the adsorption capacity of CPB modified wheat straw [18], CPB modified peanut [20], Kohlrabi peel and Rice husk [22], whereas the maximum adsorption capacities of Fe₃O₄-CTABSiO₂-NH₂ and

Fe₃O₄-SiO₂-CTABSiO₂-NH₂ are better than those of different adsorbents given in Table 4 except *Salvadora persica* (Miswak) powder [21] and PEI-modified carbon nanotubes [23]. This result can be explained by the large number of pores, in the structure of the mesoporous adsorbents prepared, the imposition of a large number of amino groups on the surface and the high affinity of LG for these amino groups [3]. As a result, the good adsorption capacities of Fe₃O₄-SiO₂-NH₂, Fe₃O₄-CTABSiO₂-NH₂ and Fe₃O₄-SiO₂-CTABSiO₂-NH₂ studied for LG removal showed that they can be used as potential adsorbents for the adsorption process.

2-5. Effect of Temperature and Adsorption Thermodynamics

In order to investigate the effect of temperature, the adsorption experiments were performed at 22, 27 and 32 °C. The results determined from the experiments are displayed in Fig. 8(a). It was observed that LG adsorption onto Fe₃O₄-SiO₂-NH₂, Fe₃O₄-CTAB-SiO₂-NH₂ and Fe₃O₄-SiO₂-CTABSiO₂-NH₂ increases with increasing the dye solution temperature. This finding can be explained by the formation of bonds between the active sites used for adsorp-

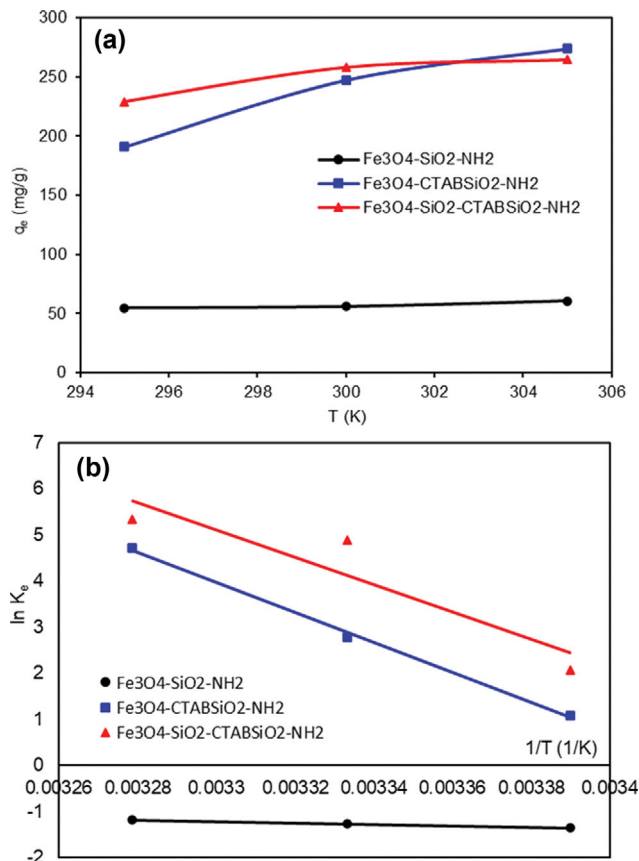


Fig. 8. (a) Effect of temperature on LG adsorption and (b) plot of $1/T$ vs. $\ln K_e$ for the adsorption of LG onto Fe₃O₄-SiO₂-NH₂, Fe₃O₄-CTABSiO₂-NH₂ and Fe₃O₄-SiO₂-CTABSiO₂-NH₂ (initial concentration: 20 mg/L, solution volume: 100 mL, agitation rate: 500 rpm, adsorbent dosage: 7 mg, pH: (3.48±0.02)).

tion on the surfaces of nanocomposites and the LG molecules, and as a result, the increase in adsorption forces also.

The thermodynamic parameters for LG adsorption onto Fe₃O₄-SiO₂-NH₂, Fe₃O₄-CTABSiO₂-NH₂ and Fe₃O₄-SiO₂-CTABSiO₂-NH₂ were calculated from equilibrium data obtained at 22, 27 and 32 °C. The values of the change in enthalpy (ΔH°), entropy (ΔS°) and Gibbs free energy (ΔG°), were obtained from Eqs. (10)-(12) [22]:

$$K_e = \frac{C_{ad,e}}{C_e} \quad (10)$$

$$\ln K_e = \frac{\Delta S^\circ}{R} - \frac{\Delta H^\circ}{RT} \quad (11)$$

$$\Delta G^\circ = \Delta H^\circ - T\Delta S^\circ \quad (12)$$

where $C_{ad,e}$ is LG concentration adsorbed on the adsorbent at equilibrium condition (mg L⁻¹). The values of ΔS° and ΔH° were obtained from the intercept and the slope of the plot of $\ln K_e$ vs. $1/T$ (Fig. 8(b)), respectively. The ΔG° for LG adsorption was calculated from Eq. (12).

The thermodynamic parameters determined for LG adsorption were given in Table 5. It was found that the adsorption of LG was spontaneous due to the negative ΔG° values determined for Fe₃O₄-CTABSiO₂-NH₂ and Fe₃O₄-SiO₂-CTABSiO₂-NH₂. The increase of the ΔG° value as temperature rises implied that the affinity of Fe₃O₄-CTABSiO₂-NH₂ and Fe₃O₄-SiO₂-CTABSiO₂-NH₂ to LG increased at high solution temperature. However, the positive values of ΔG° determined for Fe₃O₄-SiO₂-NH₂ implied that LG adsorption was non-spontaneous and there was an energy barrier and the hydration of the ions in the solution phase may be partly responsible for the energy barrier in the active state [42,43]. The positive values of ΔH° and ΔS° for all adsorbents implied that LG adsorption is endothermic progression and the randomness raised at the solution/solid interface in the process. In physisorption, ΔH° is generally below 80 kJ mol⁻¹, whereas ΔH° is in the range of 80-420 kJ mol⁻¹ in chemisorption [44]. The high values of ΔH° calculated for Fe₃O₄-CTABSiO₂-NH₂ and Fe₃O₄-SiO₂-CTABSiO₂-NH₂ except Fe₃O₄-SiO₂-NH₂ reflected that LG adsorption process involves strong forces of attraction due to the chemical nature.

2-6. Adsorption Mechanism

According to the results, the values of q_e determined for Fe₃O₄-CTABSiO₂-NH₂ and Fe₃O₄-SiO₂-CTABSiO₂-NH₂ are bigger than that of Fe₃O₄-SiO₂-NH₂ under the same experimental conditions. This observation showed that adsorption capacities of Fe₃O₄-CTABSiO₂-NH₂ and Fe₃O₄-SiO₂-CTABSiO₂-NH₂ for LG increased significantly after their modification with CTAB. The different adsorbents modified with cationic surfactant are used for LG adsorption from aqueous solutions in recent years [18,20,22]. CTAB is a cationic surfactant with quaternary ammonium structure and often

Table 5. Thermodynamic parameters of LG adsorption onto Fe₃O₄-SiO₂-NH₂, Fe₃O₄-CTABSiO₂-NH₂ and Fe₃O₄-SiO₂-CTABSiO₂-NH₂

Adsorbents	Temperature (K)	ΔG° (kJ/mol)	ΔH° (kJ/mol)	ΔS° (J/molK)	R ²
Fe ₃ O ₄ -SiO ₂ -NH ₂	295	+3.32	13.00	32.84	0.9941
	300	+3.15			
	305	+2.99			
Fe ₃ O ₄ -CTABSiO ₂ -NH ₂	295	-2.56	271.18	927.93	0.9976
	300	-7.20			
	305	-11.84			
Fe ₃ O ₄ -SiO ₂ -CTABSiO ₂ -NH ₂	295	-5.97	246.50	855.84	0.8600
	300	-10.25			
	305	-14.53			

used to produce various mesoporous silica molecular sieves under basic situations [8]. In this study, the produced mesoporous structure decreased the adsorption equilibrium time and increased the adsorption capacity due to by decreasing the diffusion resistance and enhancing the number of accessible active sites for LG molecules [45]. Similar results were reported in previously studies for adsorption of various pollutants onto mesoporous CTAB-functionalized magnetic adsorbents [8,24,45]. The functional groups on the silica-coated core-shell magnetite nanoparticles interact with dye molecules in aqueous solution, increasing the adsorption capacity, selectivity and effectiveness of them. The use of amino group as a functional group in these nanoparticles allows the anionic dye to be adsorbed by protonation of amino group at low pH [3]. Therefore, both CTAB and $-NH_2$ should be held responsible for the adsorptive interactions in explaining the adsorption mechanism.

The mechanisms for LG adsorption on $Fe_3O_4-SiO_2-NH_2$, $Fe_3O_4-CTABSiO_2-NH_2$ and $Fe_3O_4-SiO_2-CTABSiO_2-NH_2$ are ascribed to hydrogen bonding, surface complexation, ion exchange, and electrostatic attraction. The high adsorption capacities of $Fe_3O_4-CTABSiO_2-NH_2$ and $Fe_3O_4-SiO_2-CTABSiO_2-NH_2$ compared to the many adsorbents (Table 4) may be due to hydrogen bonding between N, S or O atoms of LG and O-H groups on the surface of the nanocomposites where LG molecules are bonded to the surfaces of $Fe_3O_4-CTABSiO_2-NH_2$ and $Fe_3O_4-SiO_2-CTABSiO_2-NH_2$. The driving force for the LG adsorption with $Fe_3O_4-SiO_2-NH_2$ is the electrostatic attraction between the negative charged LG ions and positively charged nanocomposite surface because of protonation of amino groups. It should be noted that the electrostatic interaction is not the dominated factor for the adsorption of LG on $Fe_3O_4-CTABSiO_2-NH_2$ and $Fe_3O_4-SiO_2-CTABSiO_2-NH_2$ but it contributes. Another mechanism to be considered for the adsorption process is the ion exchange reaction between the proton of $-OH$ or $-COOH$ functional groups and LG ions due to releasing the proton of $-OH$ or $-COOH$ into the solution during the process. It should be reported that the main driving force for LG adsorption

on $Fe_3O_4-CTABSiO_2-NH_2$ and $Fe_3O_4-SiO_2-CTABSiO_2-NH_2$ could be this ion exchange reaction. Surface complexation between LG ions and functional groups on the surfaces of the nanocomposites may be assumed a crucial role in the adsorption. The similar adsorption mechanisms for adsorption of various pollutants on mesoporous CTAB-functionalized magnetic adsorbents were reported in literature [3,8,24,45].

2-7. Structural Stability

As the nanocomposites were prepared via different routes, Fe leaching from the nanocomposites during the adsorption process was determined to figure out the difference in the stability of three nanocomposites by collecting the supernatant and analyzing using AAS. However, as the quantity of iron in the undiluted samples was below the detection limit of instrument, hence it could be assumed that the nanocomposites were highly stable under the adsorption experimental conditions and did not leach out or released any iron in the system.

To further assess the stability of the nanocomposites, FT-IR spectra of $Fe_3O_4-SiO_2-NH_2$, $Fe_3O_4-CTABSiO_2-NH_2$ and $Fe_3O_4-SiO_2-CTABSiO_2-NH_2$ nanocomposites were recorded after adsorption for LG and the results are given in Fig. 9, respectively. FT-IR spectra revealed that all adsorbents retained their innate structures after adsorption whereas the bands in the post adsorption FT-IR spectra of $Fe_3O_4-CTABSiO_2-NH_2$ and $Fe_3O_4-SiO_2-CTABSiO_2-NH_2$ adsorbents got sharper around $1,100\text{ cm}^{-1}$, which justifies the more successful adsorption of LG in comparison with $Fe_3O_4-SiO_2-NH_2$. Meanwhile, the characteristic peaks of LG appeared with noticeably around 720 cm^{-1} and 620 cm^{-1} especially in the spectra of $Fe_3O_4-CTABSiO_2-NH_2$ and $Fe_3O_4-SiO_2-CTABSiO_2-NH_2$ adsorbents, indicating that the LG does interact more intense with $Fe_3O_4-CTABSiO_2-NH_2$ and $Fe_3O_4-SiO_2-CTABSiO_2-NH_2$ adsorbents than $Fe_3O_4-SiO_2-NH_2$. In addition, the absorption peaks around 690 and $1,500\text{ cm}^{-1}$, which were ascribed to the bending vibration of $-NH$ and $-NH_2$, almost disappeared after LG adsorption especially for $Fe_3O_4-CTABSiO_2-NH_2$ and $Fe_3O_4-SiO_2-CTABSiO_2-NH_2$, which demonstrated that the amine groups on the surface of $Fe_3O_4-CTABSiO_2-$

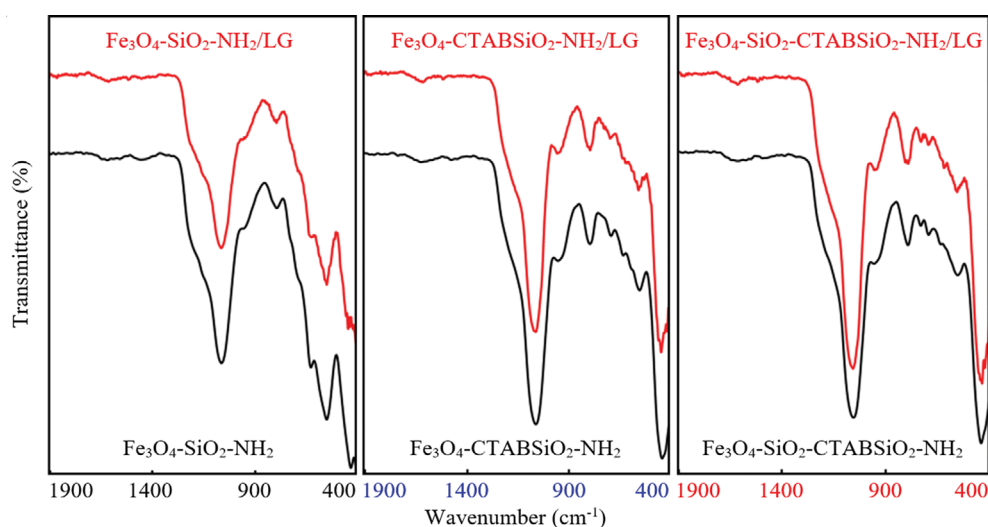


Fig. 9. Comparison of the FT-IR spectra of fresh (shown in black) and used (shown in red) nanocomposites.

NH₂ and Fe₃O₄-SiO₂-CTABSiO₂-NH₂ formed hydrogen bond with LG and this result could have also contributed to the higher adsorption properties [46].

CONCLUSIONS

In this study, the efficient and stable mesoporous Fe₃O₄-SiO₂-NH₂, Fe₃O₄-CTABSiO₂-NH₂ and Fe₃O₄-SiO₂-CTABSiO₂-NH₂ magnetic adsorbents were successfully produced and used as the new adsorbents for the adsorption of LG from aqueous solutions. In consideration of the lower density and higher porosity, a better LG removal capacity of CTAB templated Fe₃O₄-CTABSiO₂-NH₂ and Fe₃O₄-SiO₂-CTABSiO₂-NH₂ than Fe₃O₄-SiO₂-NH₂ nanocomposite was reasonable. Moreover, the quicker adsorption can be attributed to the higher affinity between the LG and CTAB modified samples than the one between LG and Fe₃O₄-SiO₂-NH₂. The adsorption data determined from batch experiments fits well with the pseudo second order kinetic model and the Langmuir isotherm, revealing that the adsorption process is homogeneous and monolayer and based on chemical interactions. The maximum adsorption capacities determined for LG adsorption of Fe₃O₄-SiO₂-NH₂, Fe₃O₄-CTABSiO₂-NH₂ and Fe₃O₄-SiO₂-CTABSiO₂-NH₂ are 56.18, 196.08 and 227.27 mg g⁻¹, respectively, which exhibit that both silica and mesoporous silica coating strategy can play very important role in improving the adsorptive properties of the adsorbents. Thermodynamic parameters determined for the adsorption process reveal that the adsorption of LG is an endothermic for all adsorbents and spontaneous process for other adsorbents except Fe₃O₄-SiO₂-NH₂. Fe₃O₄-SiO₂-NH₂, Fe₃O₄-CTABSiO₂-NH₂ and Fe₃O₄-SiO₂-CTABSiO₂-NH₂ are expected to be widely used in LG removal and may also be applied in selective separation, enrichment, and purification.

ACKNOWLEDGEMENT

This work was supported by The Commission of Scientific Research Projects of Bursa Uludag University, Project number: OUAP(F)-2015/21.

REFERENCES

1. L. Sun, S. Hu, H. Sun, H. Guo, H. Zhu, M. Liu and H. Sun, *RSC Adv*, **5**, 11837 (2015).
2. Z. Xu, W. Li, Z. Xiong, J. Fang, Y. Li, Q. Wang and Q. Zeng, *Desalin. Water Treat.*, **57**, 7054 (2016).
3. S. H. Araghi and M. H. Entezari, *Appl. Surf. Sci.*, **333**, 68 (2015).
4. A. A. Atia, A. M. Donia and W. A. Al-Amrani, *Chem. Eng. J.*, **150**, 55 (2009).
5. S.-R. Masoud, I. Mohsen, A. Somayyeh, F. Mostafa and J. Fattaneh, *J. App. Res. Wat. Wast.*, **1**, 6 (2014).
6. P. Wang, X. Wang, S. Yu, Y. Zou, J. Wang, Z. Chen, N. S. Alharbi, A. Alsaedi, T. Hayat, Y. Chen and X. Wang, *Chem. Eng. J.*, **306**, 280 (2016).
7. A. Mittal, J. Mittal, A. Malviya, D. Kaur and V. K. Gupta, *J. Colloid Interface Sci.*, **342**, 518 (2010).
8. K. Li, Z. Zeng, J. Xiong, L. Yan, H. Guo, S. Liu, Y. Dai and T. Chen, *Colloids Surf. A: Physicochem. Eng. Asp.*, **465**, 113 (2015).
9. R. Nicola, S. G. Muntean, M. A. Nistor, A. M. Putz, L. Almasy and L. Sacarescu, *Chemosphere*, **261**, 127737 (2020).
10. S. Jin, B. C. Park, W. S. Ham, L. Pan and Y. K. Kim, *Colloids Surf. A*, **531**, 133 (2017).
11. R. Nicola, O. Costişor, S. G. Muntean, M. A. Nistor, A. M. Putz, C. Ianaşi, R. Lazau, L. Almasy and L. Sacarescu, *J. Porous Mater.*, **27**, 413 (2020).
12. C. Ianaşi, M. Picioruş, R. Nicola, M. Ciopec, A. Negrea, D. Niznansky, A. Len, L. Almasy and A. M. Putz, *Korean J. Chem. Eng.*, **36**, 688 (2019).
13. J. Wang, S. Zheng, Y. Shao, J. Liu, Z. Xu and D. Zhu, *J. Colloid Interface Sci.*, **349**, 293 (2010).
14. R. Nicola, O. Costişor, M. Ciopec, A. Negrea, R. Lazau, C. Ianaşi, E. M. Picioruş, A. Len, L. Almasy, E. I. Szerb and A. M. Putz, *Appl. Sci.*, **10**, 2726 (2020).
15. Y. Deng, D. Qi, C. Deng, X. Zhang and D. Zhao, *J. Am. Chem. Soc.*, **130**, 28 (2008).
16. P. Wu, J. Zhu and Z. Xu, *Adv. Funct. Mater.*, **14**, 345 (2004).
17. W. Zhao, J. Gu, L. Zhang, H. Chen and J. Shi, *J. Am. Chem. Soc.*, **127**, 8916 (2005).
18. Y. Su, B. Zhao, W. Xiao and R. Han, *Environ. Sci. Pollut. Res.*, **20**, 5558 (2013).
19. B. Erdem, S. B. Avşar, S. Erdem and N. Tekin, *J. Dispers. Sci. Technol.*, **40**, 1227 (2019).
20. T. Zhou, W. Lu, L. Liu, H. Zhu, Y. Jiao, S. Zhang and R. Han, *J. Mol. Liq.*, **211**, 909 (2015).
21. E. A. Moawed and A. B. Abulkibash, *J. Saudi Chem. Soc.*, **20**, S178 (2016).
22. B. Zhao, W. Xiao, Y. Shang, H. Zhu and R. Han, *Arabian J. Chem.*, **10**, S3595 (2017).
23. Y. Gu, M. Liu, M. Yang, W. Wang, S. Zhang and R. Han, *Desalin. Water Treat.*, **138**, 368 (2019).
24. R. Zandipak, S. S. Ardakani and A. Shirzadi, *Sep. Sci. Technol.*, **55**, 456 (2020).
25. J. Kaur and M. Kaur, *Mater. Chem. Phys.*, **242**, 122548 (2020).
26. R. Massart, *IEEE Trans. Magn.*, **MAG-17**, 1247 (1981).
27. D. Lewandowski, M. Ceglowski, M. Smoluch, E. Reszke, J. Silbering and G. Schroeder, *Micropor. Mesopor. Mater.*, **240**, 80 (2017).
28. S. Kamari and A. Shahbazi, *Chemosphere*, **243**, 125282 (2020).
29. J. Xu, C. Ju, J. Sheng, F. Wang, Q. Zhang, G. Sun and M. Sun, *Bull. Korean Chem. Soc.*, **34**, 2408 (2013).
30. G. Fang, H. Chen, Y. Zhang and A. Chen, *Int. J. Biol. Macromol.*, **88**, 189 (2016).
31. C. Meng, W. Zhikun, L. Qiang, L. Chunling, S. Shuangqing and H. Songqing, *J. Hazard. Mater.*, **341**, 198 (2018).
32. Q. Yuan, Y. Chi, N. Yu, Y. Zhao, W. Yan, X. Li and B. Dong, *Mater. Res. Bull.*, **49**, 279 (2014).
33. Z. Kheshti, S. Hassanajili and Z. Shahrashoob, *Iran. J. Chem. Chem. Eng.*, **38**, 1 (2019).
34. S. Laurent, D. Forge, M. Port, A. Roch, C. Robic, L. V. Elst and R. N. Muller, *Chem. Rev.*, **108**, 2064 (2008).
35. F. Liu, F. Niu, N. Peng, Y. Su and Y. Yang, *RSC Adv*, **5**, 18128 (2015).
36. M. A. Betiha, Y. M. Moustafa, M. F. El-Shahat and E. Rafik, *J. Hazard. Mater.*, **397**, 122675 (2020).

37. S. A. M. K. Ansari, E. Ficiara, F. A. Ruffinatti, I. Stura, M. Argenziano, O. Abollino, R. Cavalli, C. Guiot and F. D'Agata, *Materials*, **12**, 465 (2019).
38. K. S. W. Sing, *Pure Appl. Chem.*, **54**, 2201 (1982).
39. Z. A. ALothman, *Materials*, **5**, 2874 (2012).
40. Z. Kheshti and S. Hassanajili, *J. Inorg. Organomet. Polym.*, **27**, 1613 (2017).
41. E. K. Pasandideh, B. Kakavandi, S. Nasser, A. H. Mahvi, R. Nabizadeh, A. Esrafil and R. R. Kalantary, *J. Environ. Health Sci. Eng.*, **14**, 21 (2016).
42. N. Ayar, B. Bilgin and G. Atun, *Chem. Eng. J.*, **138**, 239 (2008).
43. J. M. Salman and K. A. Al-Saad, *Int. J. Chem. Sci.*, **10**, 677 (2012).
44. M. Şölen, S. Tunali, A. S. Özcan, A. Özcan and T. Gedikbey, *Desalination*, **223**, 308 (2008).
45. R. Zandipak and S. Sobhanardakani, *Clean Technol. Environ. Policy*, **20**, 871 (2018).
46. Q. U. Ain, U. Rasheed, M. Yaseen, H. Zhang and Z. Tong, *J. Hazard. Mater.*, **397**, 122758 (2020).